CCFE
CULHAM CENTRE FOR FUSION ENERGY

UK Atomic Energy Authority

UKAEA-CCFE-PR(22)21

Hyun-Tae Kim, Francis Casson, Hendrik Meyer, Geof Cunningham, Rory Scannell, Lucy Kogan, James Harrison, Seong-Cheol Kim, Jeong-Won Lee, Jin-Woo Gwak, Yong-Su Na, Xavier Litaudon, Gloria Falchetto3, MAST team

Development of electromagnetic plasma burn-through model and validation in MAST

Development of electromagnetic plasma burn-through model and validation in MAST

Hyun-Tae Kim, Francis Casson, Hendrik Meyer, Geof Cunningham, Rory Scannell, Lucy Kogan, James Harrison, Seong-Cheol Kim, Jeong-Won Lee, Jin-Woo Gwak, Yong-Su Na, Xavier Litaudon, Gloria Falchetto3, MAST team

This is a preprint of a paper submitted for publication in Nuclear Fusion

Development of electromagnetic plasma burn-through model and validation in MAST

May 10, 2022

Hyun-Tae Kim[1], Francis Casson[1], Hendrik Meyer[1], Geof Cunningham[1], Rory Scannell[1], Lucy Kogan[1], James Harrison[1], Seong-Cheol Kim[2], Jeong-Won Lee[2], Jin-Woo Gwak[2], Yong-Su Na[2], Xavier Litaudon[3], Gloria Falchetto[3], and MAST team

[1] United Kingdom Atomic Energy Authority, Culham Science Centre, Abingdon, OX14 3DB, United Kingdom of Great Britain and Northern Ireland
[2]Department of Nuclear Engineering, Seoul National Univerisy, Seoul, Republic of Korea
[3]IRFM, CEA F-13108, Sant-Paul-lez-Durance, France

Hyun-Tae.Kim@ukaea.uk

Abstract

This paper describes the development of electromagnetic plasma burn-through model. Full circuit equations describing the currents in solenoid, poloidal field coils, and toroidally conducting passive structures have been integrated into the differential equation system of the plasma energy and particle balances in DYON. This enables consistent calculation of the time-evolving loop voltage at a plasma position only using operation signals in a control room, which are current (or voltage) waveforms in solenoid and poloidal field coils and prefill gas pressure. The synthetic flux loop data calculated in the modelling agrees well with the measurement in MAST, confirming validity of the loop voltage calculation. The electromagnetic modelling also enables calculation of 2D time-evolving poloidal magnetic flux map, thereby modelling the plasma volume evolution during the plasma break-down and burn-through phase. Only using the control room operation signals used in 34 ohmic start-up discharges with the direct induction start-up scenario in MAST, the electromagnetic plasma burn-through modelling has reproduced the time-evolution of plasma current, electron density and temperature, and plasma volume, showing a reasonable level of agreements with experimental measurement.

1 Introduction

Tokamak start-up consists of three phases: plasma break-down, plasma burn-through, and plasma current ramp-up. The induced high loop voltage or injected electromagnetic wave enables plasma break-down, generating a plasma at a low degree of ionization in a prefilled hydrogen isotope gas. Since the degree of ionization is low in this phase the electron-neutral collisions are dominant[1].

This justifies the Townsend break-down theory, which calculates the minimum toroidal electric field requried for plasma break-down $E_{Townsend}$ at a given prefill gas pressure $p(0)$ and an effective length of open magnetic field lines L_f i.e. $E_{Townsend} = \alpha(p(0))L_f$[2] where α is the mean number of collisional ionizations by an electron travelling in 1 meter (the explicit equation indicated in (17)). As the degree of ionization further increases, the energy loss rate of electrons and ions rapidly rises due to the increase in atomic reactions such as ionization, radiation, and charge exchange. This impedes the increase in T_e, and high ohmic heating power or Electron Cyclotron Heating (ECH) is required to overcome the energy loss until achieving sufficient ionization. Full ionization of Deuterium could be achieved at T_e less than 5eV[3], but fully stripping low Z impurities e.g. C^{6+}, or O^{8+} (i.e. Impurity burn-through) requires a few tens of eV[4]. After passing the peak energy loss in the plasma burn-through phase, the reduced electron energy loss enables the increase in T_e, thereby increasing plasma current with decreasing plasma resistance. Since the loop voltage or ECH power needed for sufficient plasma burn-through is much higher than that for plasma break-down, the main hurdle for successful tokamak start-up is in the plasma burn-through phase[5].

Operation scenarios for tokamak start-up are usually sought with the trial-and-error method when a new device is built. Once a few operation recipes are found in the device, the scenario is usually not further optimized. So far, this approach has not had a serious problem in present devices, although it often made a few months of delay to starting scientific experiments. However, it is likely that the approach is not enough in future devices. It is foreseen there will be a challenge in plasma initiation in ITER, which is a large superconducting device. The maximum toroidal electric field available in ITER is about 0.3 V/m[5], which is much lower than the value typically used in present devices e.g. 1 V/m in JET. In addition, the large L/R time $\tau_{L/R}$[1] resulting from the large thick vacuum vessel in ITER would make the plasma control complicated[6]. Considering about a decade of delays of ITER construction, successful immediate generation of ITER first plasma without any operational issue is of crucial importance. For this reason, it is now vital to optimize the ITER start-up scenario with reliable plasma burn-through modelling.

Plasma burn-through modelling is also important to design a new device such as Spherical Tokamak for Energy Production (STEP)[7]. In a spherical tokamak, due to the limited space and the high neutron irradiation in the centre column it is beneficial to have a thin or even no solenoid. However, this would significantly increase the uncertainty of plasma burn-through. In order to design a new spherical tokamak, it is essential to assess with numerical modelling the feasibility of plasma initiation and current ramp-up with a limited or zero loop voltage induced by the solenoid.

DYON is a plasma burn-through simulation code, developed and validated in JET with carbon wall[8] and ITER-Like wall[9], and used for ITER prediction[10]. Consistency of DYON with other mainstream plasma burn-through simulation codes, SCENPLINT[11][12][13] and BKD0[14][15][16], was verified by the code comparison conducted as a joint activity in Iternalnational Tokamak Physics Activity (ITPA) - Integrated Operating Scenario (IOS) group. Brief history of development of the plasma burn-through codes is summarized in [17], which reports the code benchmark activity. One of the main findings in [17] is that the vessel eddy currents and the evolving plasma volume could significantly affect the simulation results.

In JET modelling with DYON[8][9], the eddy current was assumed only in the structure supporting the divertor (called MK2 structure) as it is the only toroidally conducting passive structure in JET.

[1] A characteristic time for eddy currents in the vessel structures to decay i.e. $I = I_0 exp(-\frac{t}{\tau_{L/R}})$

Two circuit equations (i.e. plasma current and the eddy current in MK2) were enough to simulate JET discharges reproducing measured experimental data in the modelling. However, such simplified circuit equations might not be sufficient in other devices including ITER which has more toroidally conducting structures. With this motivation, full circuit equations describing all toroidal conducting vessel structures, solenoid, and PF coils have been integrated in DYON. The upgraded DYON not only allows proper modelling of vessel eddy currents but also calculation of loop voltage at the plasma region with the input of control room operation scenarios such as power supply voltage or coil currents. Loop voltage calculation at the plasma region is of importance as it could differ from the measured value at the vacuum vessel due to the stray field, in particular, for tokamaks with no iron core e.g. ITER.

Plasma volume is an imporant parameter in the plasma burn-through models which solve the energy and particle balance in 0D i.e. calculation of volume-averaged T_e and n_e. Since there is no measured data available in the burn-through phase, in previous modelling the plasma volume was prescribed with assumed values, which allow reproducing experimental data such as D_α emission[17]. This approach was useful to validate the plasma burn-through model, but would give a large uncertainty if the model is used to optimize operation scenario in future devices or to assess a new tokamak design. For predictive modelling, consistent calculation of plasma volume with a physics-based model is necessary. Hence, we have developed a plasma volume model in DYON. Implementation of the full circuit equations enables simulating the time-evolution of 2D poloidal magnetic flux map (i.e. ψ map) in the vacuum space. This allows assessing the Townsend break-down condition in each field line, and estimating the plasma volume.

This paper will report the development and validation of an electromagnetic plasma burn-through model where the evolving plasma volume is consistently calculated. In section 2, the development of full circuit equations and the plasma volume model are introduced. Section 3 describes ohmic plasma initiation with the direct induction scenario in MAST, and compares simulation results against experimental data from a typical direct induction discharge. With the simulation settings used to reproduce the MAST discharge, prediction capability of electromagnetic DYON simulation are assessed comparing the simulation results against 34 discharges, which were randomly selected among direct induction discharges in MAST. Section 4 provides the conclusion.

2 Development of electromagnetic plasma burn-through model

2.1 Full circuit equation

The RL circuit equation system describing electric currents in tokamaks consists of plasma current, active coil currents and induced currents in passive conducting structures, all of which are linked one another through mutual inductances. To calculate the loop voltage at the plasma region, the differential equation system of circuit equations should be solved consistently.

We could first consider the simplest case which is a single coil loop without any other coils nearby. The consumption of the coil voltage applied by external power supply V_c is decomposed into the resistive voltage ($V_R = R_c I_c$) and the inductive voltage ($V_L = \dfrac{d\psi_c}{dt}$), where I_c and R_c are the electric current and resistance in the coil loop, respectively. ψ_c is the magnetic flux enclosed by the coil loop, and is calculated as $\psi_c = L_c I_c$ where L_c is the self-inductance of the coil loop. If the coil geometry is

fixed (i.e. $\frac{dL_c}{dt} = 0$), which is the case in experiment devices, the inductive voltage can be replaced with $L_c \frac{dI_c}{dt}$:

$$V_c = V_R + V_L = R_c I_c + \frac{d\psi_c}{dt} = R_c I_c + L_c \frac{dI_c}{dt}$$

Now we consider multiple coil loops and toroidally conducting vessel structures (i.e. passive loops) nearby where magnetic fluxes are linked one another and the position of each loop is fixed. The system of circuit equations with n loops of coils and vessel structures have the following matrix form:

$$\overrightarrow{V_{cv}} = \overleftrightarrow{R_{cv}} \overrightarrow{I_{cv}} + \overleftrightarrow{M_{cv}} \frac{d\overrightarrow{I_{cv}}}{dt} \tag{1}$$

where $\overrightarrow{V_{cv}}$ is a $n \times 1$ column vector of voltage applied by external power supply, to coil loops and toroidally conducting passive structure in the vacuum vessel (hence zero for the vector elements corresponding to the vessel components). $\overleftrightarrow{R_{cv}}$ is a $n \times n$ diagonal matrix of resistances in the coil loops and the vessel components. $\overrightarrow{I_{cv}}$ is a $n \times 1$ column vector of currents in the coil loops and the vessel components. $\overleftrightarrow{M_{cv}}$ is a $n \times n$ symmetric matrix of inductances in coil loops and vessel components. In $\overleftrightarrow{M_{cv}}$, non-diagonal elements and diagonal elements are mutual inductance and self-inductance, respectively.

In order to include the plasma current, (1) is extended by attaching the plasma current I_p in the $(n+1)$th row of the corresponding column vectors. In other words, $\overrightarrow{V_{cv}}$ and $\overrightarrow{I_{cv}}$ are extended to $\overrightarrow{V_{cvp}}$ and $\overrightarrow{I_{cvp}}$, which are $(n+1) \times 1$ column vectors. The plasma resistance R_p is added in the $(n+1, n+1)$ element of $\overleftrightarrow{R_{cv}}$. The mutual inductances between I_p and both coils and vessel components are attached in the $(n+1)$th row and column of $\overleftrightarrow{M_{cv}}$, and the plasma self-inductance is added in the $(n+1, n+1)$ element. The extended mutual inductance matrix is $\overleftrightarrow{M_{cvp}}$, which is a $(n+1) \times (n+1)$ matrix. $\overrightarrow{I_{cvp}}$,

$\overrightarrow{V_{cvp}}$, $\overleftrightarrow{R_{cvp}}$, and $\overleftrightarrow{M_{cvp}}$ can be explicitly written as

$$\overrightarrow{I_{cvp}} = \begin{bmatrix} I_{c1} \\ I_{c2} \\ \vdots \\ I_{v1} \\ I_{v2} \\ \vdots \\ I_p \end{bmatrix}, \overrightarrow{V_{cvp}} = \begin{bmatrix} V_{c1} \\ V_{c2} \\ \vdots \\ V_{v1} \\ V_{v2} \\ \vdots \\ V_{plasma} \end{bmatrix} = \begin{bmatrix} V_{c1} \\ V_{c2} \\ \vdots \\ 0 \\ 0 \\ \vdots \\ 0 \end{bmatrix}, \overleftrightarrow{R_{cvp}} = \begin{bmatrix} R_{c1} & 0 & \cdots & 0 & 0 & \cdots & 0 \\ 0 & R_{c2} & \cdots & 0 & 0 & \cdots & 0 \\ \vdots & \vdots & \ddots & \vdots & \vdots & \cdots & \vdots \\ 0 & 0 & \cdots & R_{v1} & 0 & \cdots & 0 \\ 0 & 0 & \cdots & 0 & R_{v2} & \cdots & 0 \\ \vdots & \vdots & \vdots & \vdots & \vdots & \ddots & \vdots \\ 0 & 0 & \cdots & 0 & 0 & \cdots & R_p \end{bmatrix}$$

$$\overleftrightarrow{M_{cvp}} = \begin{bmatrix} L_{c1} & M_{c1,c2} & M_{c1,c3} & \cdots & M_{c1,v1} & M_{c1,v2} & M_{c1,v3} & \cdots & M_{c1,p} \\ M_{c2,c1} & L_{c2} & M_{c2,c3} & \cdots & M_{c2,v1} & M_{c2,v2} & M_{c2,v3} & \cdots & M_{c2,p} \\ M_{c3,c1} & M_{c3,c2} & L_{c3} & \cdots & M_{c3,v1} & M_{c3,v2} & M_{c3,v3} & \cdots & M_{c3,p} \\ \vdots & \vdots & \vdots & \ddots & \vdots & \vdots & \vdots & \cdots & \vdots \\ M_{v1,c1} & M_{v1,c2} & M_{v1,c3} & \cdots & L_{v1} & M_{v1,v2} & M_{v1,v3} & \cdots & M_{v1,p} \\ M_{v2,c1} & M_{v2,c2} & M_{v2,c3} & \cdots & M_{v2,v1} & L_{v2} & M_{v2,v3} & \cdots & M_{v2,p} \\ M_{v3,c1} & M_{v3,c2} & M_{v3,c3} & \cdots & M_{v3,v1} & M_{v3,v2} & L_{v3} & \cdots & M_{v3,p} \\ \vdots & \vdots & \vdots & \vdots & \vdots & \vdots & \vdots & \ddots & \vdots \\ M_{p,c1} & M_{p,c2} & M_{p,c3} & \cdots & M_{p,v1} & M_{p,v2} & M_{p,v3} & \cdots & L_p \end{bmatrix} \tag{2}$$

Compared to the circuit equation system without I_p, one of the main differences in the extended circuit equation system is that the mutual inductance could evolve in time, as the position and shape of a plasma current could change in time. This makes an additional term $\frac{d\overleftrightarrow{M_{cvp}}}{dt}\overrightarrow{I_{cvp}}$ in the extended circuit equation system as shown below:

$$\begin{aligned} \overrightarrow{V_{cvp}} &= \overleftrightarrow{R_{cvp}}\overrightarrow{I_{cvp}} + \frac{d\overleftrightarrow{M_{cvp}}\overrightarrow{I_{cvp}}}{dt} \\ &= \overleftrightarrow{R_{cvp}}\overrightarrow{I_{cvp}} + \frac{d\overleftrightarrow{M_{cvp}}}{dt}\overrightarrow{I_{cvp}} + \overleftrightarrow{M_{cvp}}\frac{d\overrightarrow{I_{cvp}}}{dt} \\ &= \big(\overleftrightarrow{R_{cvp}} + \frac{\partial\overleftrightarrow{M_{cvp}}}{\partial R}\frac{\partial R}{\partial t} + \frac{\partial\overleftrightarrow{M_{cvp}}}{\partial Z}\frac{\partial Z}{\partial t} + \frac{d\overleftrightarrow{L_p}}{dt}\big)\overrightarrow{I_{cvp}} + \overleftrightarrow{M_{cvp}}\frac{d\overrightarrow{I_{cvp}}}{dt} \end{aligned} \tag{3}$$

Note, R and Z are the radial and vertical position of each current element, respectively. All current loops are assumed to be toroidally symmetry. $\frac{\partial\overleftrightarrow{M_{cvp}}}{\partial R}\frac{\partial R}{\partial t}$ and $\frac{\partial\overleftrightarrow{M_{cvp}}}{\partial Z}\frac{\partial Z}{\partial t}$ have all zero elements except the elements corresponding to the mutual inductances of I_p with coils and vessel components i.e. the last row and column. This is because the positions of coils and vessel components are fixed (i.e. $\frac{\partial R}{\partial t} = 0$ and $\frac{\partial Z}{\partial t} = 0$), whereas I_p position could change in time (i.e. $\frac{\partial R}{\partial t} \neq 0$ and $\frac{\partial Z}{\partial t} \neq 0$). Note, $(n+1, n+1)$ element in $\frac{\partial\overleftrightarrow{M_{cvp}}}{\partial R}\frac{\partial R}{\partial t}$ and $\frac{\partial\overleftrightarrow{M_{cvp}}}{\partial Z}\frac{\partial R}{\partial t}$ is defined as zero. This is because the plasma self-inductance is not only a function of the radial position R and vertial position Z but also of the minor radius and elongation. Hence, the time derivative of plasma self-inductance is included as a

separate $(n+1)\times(n+1)$ matrix $\dfrac{d\overleftrightarrow{L_p}}{dt}$, where $(n+1,n+1)$ element is the time derivative of plasma self-inductance i.e. $\frac{dL_p}{dt}$, and all the other elements are zero. L_p is calculated with the evolving plasma parameters from the plasma volume model, which will be introduced in section 2.2. (3) is equivalent to the following explicit matrix presentation:

$$\begin{bmatrix} V_{c1} \\ V_{c2} \\ \vdots \\ 0 \\ 0 \\ \vdots \\ 0 \end{bmatrix} = \begin{bmatrix} L_{c1} & M_{c1,c2} & M_{c1,c3} & \cdots & M_{c1,v1} & M_{c1,v2} & M_{c1,v3} & \cdots & M_{c1,p} \\ M_{c2,c1} & L_{c2} & M_{c2,c3} & \cdots & M_{c2,v1} & M_{c2,v2} & M_{c2,v3} & \cdots & M_{c2,p} \\ M_{c3,c1} & M_{c3,c2} & L_{c3} & \cdots & M_{c3,v1} & M_{c3,v2} & M_{c3,v3} & \cdots & M_{c3,p} \\ \vdots & \vdots & \vdots & \ddots & \vdots & \vdots & \vdots & \cdots & \vdots \\ M_{v1,c1} & M_{v1,c2} & M_{v1,c3} & \cdots & L_{v1} & M_{v1,v2} & M_{v1,v3} & \cdots & M_{v1,p} \\ M_{v2,c1} & M_{v2,c2} & M_{v2,c3} & \cdots & M_{v2,v1} & L_{v2} & M_{v2,v3} & \cdots & M_{v2,p} \\ M_{v3,c1} & M_{v3,c2} & M_{v3,c3} & \cdots & M_{v3,v1} & M_{v3,v2} & L_{v3} & \cdots & M_{v3,p} \\ \vdots & \vdots & \vdots & \vdots & \vdots & \vdots & \vdots & \ddots & \vdots \\ M_{p,c1} & M_{p,c2} & M_{p,c3} & \cdots & M_{p,v1} & M_{p,v2} & M_{p,v3} & \cdots & L_p \end{bmatrix} \begin{bmatrix} \frac{dI_{c1}}{dt} \\ \frac{dI_{c2}}{dt} \\ \frac{dI_{c3}}{dt} \\ \vdots \\ \frac{dI_{v1}}{dt} \\ \frac{dI_{v2}}{dt} \\ \frac{dI_{v3}}{dt} \\ \vdots \\ \frac{dI_p}{dt} \end{bmatrix}$$

$$+ \begin{bmatrix} R_{c1} & 0 & \cdots & 0 & 0 & \cdots & \frac{\partial M_{c1,p}}{\partial R}\frac{\partial R}{\partial r} + \frac{\partial M_{c1,p}}{\partial Z}\frac{\partial Z}{\partial t} \\ 0 & R_{c2} & \cdots & 0 & 0 & \cdots & \frac{\partial M_{c2,p}}{\partial R}\frac{\partial R}{\partial r} + \frac{\partial M_{c2,p}}{\partial Z}\frac{\partial Z}{\partial t} \\ \vdots & \vdots & \ddots & \vdots & \vdots & \cdots & \vdots \\ 0 & 0 & \cdots & R_{v1} & 0 & \cdots & \frac{\partial M_{v1,p}}{\partial R}\frac{\partial R}{\partial r} + \frac{\partial M_{v1,p}}{\partial Z}\frac{\partial Z}{\partial t} \\ 0 & 0 & \cdots & 0 & R_{v2} & \cdots & \frac{\partial M_{v2,p}}{\partial R}\frac{\partial R}{\partial r} + \frac{\partial M_{v2,p}}{\partial Z}\frac{\partial Z}{\partial t} \\ \vdots & \vdots & \vdots & \vdots & \vdots & \ddots & \vdots \\ \frac{\partial M_{c1,p}}{\partial R}\frac{\partial R}{\partial r} + \frac{\partial M_{c1,p}}{\partial Z}\frac{\partial Z}{\partial t} & \cdots & \cdots & \frac{\partial M_{v1,p}}{\partial R}\frac{\partial R}{\partial r} + \frac{\partial M_{v1,p}}{\partial Z}\frac{\partial Z}{\partial t} & \cdots & \cdots & R_p + \frac{dL_p}{dt} \end{bmatrix} \begin{bmatrix} I_{c1} \\ I_{c2} \\ \vdots \\ I_{v1} \\ I_{v2} \\ \vdots \\ I_p \end{bmatrix} \tag{4}$$

Rearranging (3) for $\dfrac{d\overrightarrow{I_{cvp}}}{dt}$, the differential equation system describing all toroidal currents in a tokamak is derived,

$$\frac{d\overrightarrow{I_{cvp}}}{dt} = \overleftrightarrow{M_{cvp}}^{-1}\Big(\overrightarrow{V_{cvp}} - \big(\overleftrightarrow{R_{cvp}} + \frac{\partial\overleftrightarrow{M_{cvp}}}{\partial R}\frac{\partial R}{\partial t} + \frac{\partial\overleftrightarrow{M_{cvp}}}{\partial Z}\frac{\partial Z}{\partial t} + \frac{d\overleftrightarrow{L_p}}{dt}\big)\overrightarrow{I_{cvp}}\Big) \tag{5}$$

If the power supply voltage applied to each coil is available to use as input data, the elements corresponding to coils in $\overrightarrow{V_{cvp}}$ (i.e. $V_{c1}, V_{c2}, \cdots$) are directly given while the other elements for vessel components and the plasma current are zero. In this case, (5) can be solved for $\dfrac{d\overrightarrow{I_{cvp}}}{dt}$. However, it is more common in tokamaks that the coil current data is available to use, rather than the power supply voltage data, as the currents are easier to rountinely measure. In the case of using coil current as input data (i.e. $\overrightarrow{I_c}$ and $\dfrac{d\overrightarrow{I_c}}{dt}$), the vessel currents and plasma current (i.e. $\dfrac{d\overrightarrow{I_{vp}}}{dt}$) are calculated by

solving a subset of (4) corresponding to the vessel components and plasma current:

$$\begin{bmatrix}0\\0\\\vdots\\0\end{bmatrix} = \begin{bmatrix} M_{v1,c1} & M_{v1,c2} & M_{v1,c3} & \cdots & L_{v1} & M_{v1,v2} & M_{v1,v3} & \cdots & M_{v1,p} \\ M_{v2,c1} & M_{v2,c2} & M_{v2,c3} & \cdots & M_{v2,v1} & L_{v2} & M_{v2,v3} & \cdots & M_{v2,p} \\ M_{v3,c1} & M_{v3,c2} & M_{v3,c3} & \cdots & M_{v3,v1} & M_{v3,v2} & L_{v3} & \cdots & M_{v3,p} \\ \vdots & \vdots & \vdots & \vdots & \vdots & \vdots & \vdots & \ddots & \vdots \\ M_{p,c1} & M_{p,c2} & M_{p,c3} & \cdots & M_{p,v1} & M_{p,v2} & M_{p,v3} & \cdots & L_p \end{bmatrix} \begin{bmatrix} \frac{dI_{c1}}{dt} \\ \frac{dI_{c2}}{dt} \\ \frac{dI_{c3}}{dt} \\ \vdots \\ \frac{dI_{v1}}{dt} \\ \frac{dI_{v2}}{dt} \\ \frac{dI_{v3}}{dt} \\ \vdots \\ \frac{dI_p}{dt} \end{bmatrix}$$

$$+ \begin{bmatrix} 0 & 0 & \cdots & R_{v1} & 0 & \cdots & \frac{\partial M_{v1,p}}{\partial R}\frac{\partial R}{\partial r} + \frac{\partial M_{v1,p}}{\partial Z}\frac{\partial Z}{\partial t} \\ 0 & 0 & \cdots & 0 & R_{v2} & \cdots & \vdots \\ \vdots & \vdots & \vdots & \vdots & \vdots & \ddots & \vdots \\ \frac{\partial M_{c1,p}}{\partial R}\frac{\partial R}{\partial r} + \frac{\partial M_{c1,p}}{\partial Z}\frac{\partial Z}{\partial t} & \cdots & \cdots & \frac{\partial M_{v1,p}}{\partial R}\frac{\partial R}{\partial r} + \frac{\partial M_{v1,p}}{\partial Z}\frac{\partial Z}{\partial t} & \cdots & \cdots & R_p + \frac{dL_p}{dt} \end{bmatrix} \begin{bmatrix} I_{c1} \\ I_{c2} \\ \vdots \\ I_{v1} \\ I_{v2} \\ \vdots \\ I_p \end{bmatrix} \tag{6}$$

Since there is no power supply directly connected to vessel components and I_p, the column vector in the left-hand-side of (6) is zero. Splitting the first term in the right-hand-side of (6) into two parts related to $\frac{d\overrightarrow{I_c}}{dt}$ and $\frac{d\overrightarrow{I_{vp}}}{dt}$, we can rewrite (6) as

$$\begin{bmatrix}0\\0\\0\\0\end{bmatrix} = \begin{bmatrix} M_{v1,c1} & M_{v1,c2} & M_{v1,c3} & \cdots \\ M_{v2,c1} & M_{v2,c2} & M_{v2,c3} & \cdots \\ M_{v3,c1} & M_{v3,c2} & M_{v3,c3} & \cdots \\ \vdots & \vdots & \vdots & \vdots \\ M_{p,c1} & M_{p,c2} & M_{p,c3} & \cdots \end{bmatrix} \begin{bmatrix} \frac{dI_{c1}}{dt} \\ \frac{dI_{c2}}{dt} \\ \frac{dI_{c3}}{dt} \\ \vdots \end{bmatrix} + \overbrace{\begin{bmatrix} L_{v1} & M_{v1,v2} & M_{v1,v3} & \cdots & M_{v1,p} \\ M_{v2,v1} & L_{v2} & M_{v2,v3} & \cdots & M_{v2,p} \\ M_{v3,v1} & M_{v3,v2} & L_{v3} & \cdots & M_{v3,p} \\ \vdots & \vdots & \ddots & \vdots & \vdots \\ M_{p,v1} & M_{p,v2} & M_{p,v3} & \cdots & L_p \end{bmatrix}}^{=\overleftrightarrow{M_{vp}}} \begin{bmatrix} \frac{dI_{v1}}{dt} \\ \frac{dI_{v2}}{dt} \\ \frac{dI_{v3}}{dt} \\ \vdots \\ \frac{dI_p}{dt} \end{bmatrix}$$

$$+ \begin{bmatrix} 0 & 0 & \cdots & R_{v1} & 0 & \cdots & \frac{\partial M_{v1,p}}{\partial R}\frac{\partial R}{\partial r} + \frac{\partial M_{v1,p}}{\partial Z}\frac{\partial Z}{\partial t} \\ 0 & 0 & \cdots & 0 & R_{v2} & \cdots & \vdots \\ \vdots & \vdots & \vdots & \vdots & \vdots & \ddots & \vdots \\ \frac{\partial M_{c1,p}}{\partial R}\frac{\partial R}{\partial r} + \frac{\partial M_{c1,p}}{\partial Z}\frac{\partial Z}{\partial t} & \cdots & \cdots & \frac{\partial M_{v1,p}}{\partial R}\frac{\partial R}{\partial r} + \frac{\partial M_{v1,p}}{\partial Z}\frac{\partial Z}{\partial t} & \cdots & \cdots & R_p + \frac{dL_p}{dt} \end{bmatrix} \begin{bmatrix} I_{c1} \\ I_{c2} \\ \vdots \\ I_{v1} \\ I_{v2} \\ \vdots \\ I_p \end{bmatrix} \tag{7}$$

Rearranging (7) to solve for $\frac{d\overrightarrow{I_{vp}}}{dt}$, the following differential equation system is derived:

$$\begin{bmatrix} \frac{dI_{v1}}{dt} \\ \frac{dI_{v2}}{dt} \\ \frac{dI_{v3}}{dt} \\ \vdots \\ \frac{dI_p}{dt} \end{bmatrix} = -\overleftrightarrow{M_{vp}}^{-1} \begin{bmatrix} M_{v1,c1} & M_{v1,c2} & M_{v1,c3} & \cdots \\ M_{v2,c1} & M_{v2,c2} & M_{v2,c3} & \cdots \\ M_{v3,c1} & M_{v3,c2} & M_{v3,c3} & \cdots \\ \vdots & \vdots & \vdots & \vdots \\ M_{p,c1} & M_{p,c2} & M_{p,c3} & \cdots \end{bmatrix} \begin{bmatrix} \frac{dI_{c1}}{dt} \\ \frac{dI_{c2}}{dt} \\ \frac{dI_{c3}}{dt} \\ \vdots \end{bmatrix}$$

$$-\overleftrightarrow{M_{vp}}^{-1} \begin{bmatrix} 0 & 0 & \cdots & R_{v1} & 0 & \cdots & \frac{\partial M_{v1,p}}{\partial R}\frac{\partial R}{\partial r} + \frac{\partial M_{v1,p}}{\partial Z}\frac{\partial Z}{\partial t} \\ 0 & 0 & \cdots & 0 & R_{v2} & \cdots & \vdots \\ \vdots & \vdots & \vdots & \vdots & \vdots & \ddots & \vdots \\ \frac{\partial M_{c1,p}}{\partial R}\frac{\partial R}{\partial r} + \frac{\partial M_{c1,p}}{\partial Z}\frac{\partial Z}{\partial t} & \cdots & \cdots & \frac{\partial M_{v1,p}}{\partial R}\frac{\partial R}{\partial r} + \frac{\partial M_{v1,p}}{\partial Z}\frac{\partial Z}{\partial t} & \cdots & \cdots & R_p + \frac{dL_p}{dt} \end{bmatrix} \begin{bmatrix} I_{c1} \\ I_{c2} \\ \vdots \\ I_{v1} \\ I_{v2} \\ \vdots \\ I_p \end{bmatrix} \tag{8}$$

Note, the last row of $\frac{d\overrightarrow{I_{cvp}}}{dt}$ in (5) or $\frac{d\overrightarrow{I_{vp}}}{dt}$ in (8) correspond to the circuit equation for I_p, which can also be explicitly written:

$$0 = R_p I_p + \frac{dL_p I_p}{dt} + \frac{d\psi_{cv}}{dt} = R_p I_p + L_p \frac{dI_p}{dt} + \frac{dL_p}{dt} I_p - V_{loop} \tag{9}$$

V_{loop} is the loop voltage induced to I_p by the coil currents and vessel eddy currents, and is calculated as $-\frac{d\psi_{cv}}{dt}$, which is a $n \times 1$ column vector of the magnetic flux induced by the time evolution of the currents in coils and vessel components. Rearranging (9), we can get the differential equation for $\frac{dI_p}{dt}$ as follows,

$$\frac{dI_p}{dt} = \frac{1}{L_p}\Big(V_{loop} - R_p I_p - \frac{dL_p}{dt} I_p\Big) \tag{10}$$

where

$$V_{loop} \equiv -\frac{d\overrightarrow{\psi_{cv}}}{dt} = \frac{d\overrightarrow{M_p}^T \overrightarrow{I_{cv}}}{dt} = -(\overrightarrow{M_p}^T \frac{d\overrightarrow{I_{cv}}}{dt} + \frac{\partial \overrightarrow{M_p}^T}{\partial R}\frac{\partial R}{\partial t}\overrightarrow{I_{cv}} + \frac{\partial \overrightarrow{M_p}^T}{\partial Z}\frac{\partial Z}{\partial t}\overrightarrow{I_{cv}}) \tag{11}$$

$\overrightarrow{M_p}^T$ is the transpose of a $n \times 1$ column vector $\overrightarrow{M_p}$, which corresponds to the mutual inductance of I_p with coils and vessel components.

The plasma current position R and Z could be calculated by solving radial and vertical force balance equations, but in the present modelling they are prescribed by input data. The plasma self-inductance L_p is a function of plasma volume geometry i.e. major radius R_{vol}, minor radius r_{vol}, and elongation, which is calculated by the plasma volume model (described in the next section). In

addition to the plasma geometry, calculation of plasma resistance R_p needs T_e and Z_{eff}. Depending on the input data availability, either (5) or (8) is solved together with the existing differential equation system in DYON. This enables consistent calculation of I_p and currents in the coils and the vacuum components with time-evolving R_p. Following is the summary of the differential equation system in DYON, which describes the plasma energy and particle balance. More details about DYON can be found in [8][9][10][17][18][19].

$$
\begin{aligned}
\frac{3}{2}\frac{d(n_eT_e)}{dt} &= P_{oh} + P_{aux} - (P_{iz} + P_{rad}) - P_{equi} - P_{econ} \\
\frac{3}{2}\frac{d(n_iT_i)}{dt} &= P_{equi} - P_{CX} - P_{icon} \\
\frac{dn_D^0}{dt} &= \frac{1}{\gamma_n^D V_V}(V_p < \sigma v >_{D,rec}^{1+\rightarrow 0} n_e n_D^{1+} - V_n^D < \sigma v >_{D,iz}^{0\rightarrow 1+} n_e n_D^0 \\
&\quad - V_n^D \sum_I \sum_{z\geq 1} < \sigma v >_{I,cx}^{z+\rightarrow (z-1)+} n_D^0 n_I^{z+}) + \frac{\Gamma_{D,in}^{total}}{\gamma_n^D V_V} \\
\frac{dn_D^{1+}}{dt} &= \frac{V_n^D}{V_p} < \sigma v >_{D,iz}^{0\rightarrow 1+} n_e n_D^0 - < \sigma v >_{D,rec}^{1+\rightarrow 0} n_e n_D^{1+} \\
&\quad + \frac{V_n^D}{V_p} \sum_I \sum_{z\geq 1} < \sigma v >_{I,cx}^{z+\rightarrow (z-1)+} n_D^0 n_I^{z+} - \frac{n_D^{1+}}{\tau_D} - \frac{n_D^{1+}}{V_p}\frac{dV_p}{dt} \\
\frac{dn_I^0}{dt} &= -\frac{V_n^I}{\gamma_n^I V_V} < \sigma v >_{I,iz}^{0\rightarrow 1+} n_e n_I^0 + \frac{V_p}{\gamma_n^I V_V} < \sigma v >_{I,rec}^{1+\rightarrow 0} n_e n_I^{1+} \\
&\quad + \frac{V_n^D}{\gamma_n^I V_V} < \sigma v >_{I,cx}^{1+\rightarrow 0} n_D^0 n_I^{1+} + \frac{\Gamma_{I,in}^0}{\gamma_n^I V_V} \\
\frac{dn_I^{1+}}{dt} &= \frac{V_n^I}{V_p} < \sigma v >_{I,iz}^{0\rightarrow 1+} n_e n_I^0 - < \sigma v >_{I,iz}^{1\rightarrow 2+} n_e n_I^{1+} + < \sigma v >_{I,rec}^{2+\rightarrow 1+} n_e n_I^{2+} - < \sigma v >_{I,rec}^{1+\rightarrow 0} n_e n_I^{1+} \\
&\quad + \frac{V_n^D}{V_p} < \sigma v >_{I,cx}^{2+\rightarrow 1+} n_D^0 n_I^{2+} - \frac{V_n^D}{V_p} < \sigma v >_{I,cx}^{1+\rightarrow 0} n_D^0 n_I^{1+} - \frac{n_I^{1+}}{\tau_I} - \frac{n_I^{1+}}{V_p}\frac{dV_p}{dt} \\
\frac{dn_I^{z+}}{dt} &= < \sigma v >_{I,iz}^{(z-1)+\rightarrow z+} n_e n_I^{(z-1)+} - < \sigma v >_{I,iz}^{z+\rightarrow (z+1)+} n_e n_I^{z+} + < \sigma v >_{I,rec}^{(z+1)+\rightarrow z+} n_e n_I^{(z+1)+} \\
&\quad - < \sigma v >_{I,rec}^{z+\rightarrow (z-1)+} n_e n_I^{z+} + \frac{V_n^D}{V_p} < \sigma v >_{I,cx}^{(z+1)+\rightarrow z+} n_D^0 n_I^{(z+1)+} \\
&\quad - \frac{V_n^D}{V_p} < \sigma v >_{I,cx}^{z+\rightarrow (z-1)+} n_D^0 n_I^{z+} - \frac{n_I^{z+}}{\tau_I} - \frac{n_I^{z+}}{V_p}\frac{dV_p}{dt}
\end{aligned}
\tag{12}
$$

2.2 Plasma volume model

ψ in each mesh grid cell in the vacuum space i.e. R_{grid} and Z_{grid} can be calculated with coil currents $I_{c\#}$, vessel eddy currents $I_{v\#}$, and plasma current I_p, of which the radial and vertical positions are

R and Z. Mutual inductances are determined by the relative position between each mesh grid and current i.e. $M(R_{grid}, Z_{grid}, R_{current}, Z_{current})$. ψ in each mesh grid is then calculated as the sum of the contributions from all currents :

$$\begin{aligned}\psi(R_{grid}, Z_{grid}) = &\sum_{c\#} M(R_{grid}, Z_{grid}, R', Z') I_{c\#}(R', Z') \\ &+ \sum_{v\#} M(R_{grid}, Z_{grid}, R'', Z'') I_{v\#}(R'', Z'') \\ &+ M(R_{grid}, Z_{grid}, R, Z) I_p(R, Z)\end{aligned} \tag{13}$$

The radial and vertical magnetic fields and the induced loop voltage (and toroidal electric field) in each mesh grid cell are calculated by derivatives of $\psi(R_{grid}, Z_{grid})$ with respect to R_{grid}, Z_{grid}, and time, respectively:

$$\begin{aligned}B_R(R_{grid}, Z_{grid}) &= -\frac{1}{2\pi R_{grid}} \frac{\partial \psi(R_{grid}, Z_{grid})}{\partial Z_{grid}} \\ B_Z(R_{grid}, Z_{grid}) &= \frac{1}{2\pi R_{grid}} \frac{\partial \psi(R_{grid}, Z_{grid})}{\partial R_{grid}} \\ V_{loop}(R_{grid}, Z_{grid}) &= -\sum_{c\#} M(R_{grid}, Z_{grid}, R', Z') \frac{I_{c\#}(R', Z')}{dt} \\ &\quad - \sum_{v\#} M(R_{grid}, Z_{grid}, R'', Z'') \frac{I_{v\#}(R'', Z'')}{dt} \\ &\quad - M(R_{grid}, Z_{grid}, R, Z) \frac{I_p(R, Z)}{dt} \\ &\quad - \frac{\partial M(R_{grid}, Z_{grid}, R, Z)}{\partial R_{grid}} \frac{\partial R}{\partial t} I_p(R, Z) \\ &\quad - \frac{\partial M(R_{grid}, Z_{grid}, R, Z)}{\partial Z_{grid}} \frac{\partial Z}{\partial t} I_p(R, Z) \\ E_\phi(R_{grid}, Z_{grid}) &= \frac{V_{loop}(R_{grid}, Z_{grid})}{2\pi R_{grid}}\end{aligned} \tag{14}$$

$B_R(R_{grid}, Z_{grid})$ and $B_Z(R_{grid}, Z_{grid})$ in (14) and the toroidal magnetic field $B_\phi(R_{grid}, Z_{grid})(= \frac{B_\phi(R_0) R_0}{R}$, where R_0 is the major radius to the vacuum centre.) enables the field-line-following calculation. In other words, if $R_{grid,k}$ and $Z_{grid,k}$ are the radial and vertical position at kth point on an open magnetic field line, we can calculate the next mesh grid point after traveling a step length Δl along the field line i.e. $R_{grid,k+1}$ and $Z_{grid,k+1}$.

$$\begin{aligned}R_{grid,k+1} &= R_{grid,k} + \frac{B_{R,k}}{\sqrt{{B_{R,k}}^2 + {B_{Z,k}}^2 + {B_{\phi,k}}^2}} \Delta l \\ Z_{grid,k+1} &= Z_{grid,k} + \frac{B_{Z,k}}{\sqrt{{B_{R,k}}^2 + {B_{Z,k}}^2 + {B_{\phi,k}}^2}} \Delta l\end{aligned} \tag{15}$$

Here, Δl is a constant length, and it should be sufficiently short considering the curvature of field lines. If not, the mesh grid points calculated with the field-line-following could deviate from the field line. However, too short Δl would require unnecessarily significant computation time. For MAST simulations, 5cm is enough to follow the field lines. $k = 1$ and $k = N$ indicate the starting point and the end point of the field-line-following calculation, respectively. Thus, in an open field line, $k = 1$ and $k = N$ corresponds to each grid point arriving at the vessel wall, while in a closed field line, $k = N$ is at the same grid point as $k = 1$ after one poloidal turn of the field line. Since the total number of points of field-line-following calculations in a field line is N, for open field lines the connection length of the field line is calculated as $L_{open} = N\Delta l$, and this allows the calculation of the averaged electric field parallel to the magnetic field.

$$\begin{aligned} E_{\parallel}(R_{grid,k}, Z_{grid,k}) &= \frac{B_{\phi,k}}{\sqrt{B_{\phi,k}^2 + B_{R,k}^2 + B_{Z,k}^2}} E_{\phi}(R_{grid,k}, Z_{grid,k}) \\ < E_{\parallel} > &= \frac{\sum_{k=1}^{k=N} E_{\parallel(R_{grid,k}, Z_{grid,k})}}{N} \end{aligned} \tag{16}$$

For open field lines, $< E_{\parallel} >$ is compared to the *Townsend electric field* $E_{Townsend}$, which is the minimum electric field required for *Townsend break-down* to take place[5].

$$E_{Townsend}[V/m] = \frac{1.25 \times 10^4 p[Torr]}{\ln\left(510 p[Torr] L_{open}[m]\right)} = \frac{93.758 \times p[Pa]}{\ln\left(3.8253 p[Pa] L_{open}[m]\right)} \tag{17}$$

$< E_{\parallel} >$ in all magnetic field lines crossing the mid-plane are individually compared with $E_{Townsend}$. Figure 1 is an example of this assessment in a MAST discharge #27512, which will be used to validate the electromagnetic burn-through model in the next section. The solid lines with different colors in Figure 1(a) indicate $E_{Townsend}$ in each open magnetic field line crossing different major radius positions on the mid-plane, which are calculated by (17). L_{open} was calculated with the field-line-following in (15), and p was measured at 3ms when plasma break-down first occurs. $< E_{\parallel} >$ in the field lines are indicated by triangles with the same color as the corresponding solid lines. L_{open} and the major radius on the mid-plane in each field line are shown in the legend. Towards the high field side, $E_{Townsend}$ are reduced as L_{open} increases. Although the poloidal field null is near the vessel centre ($R \sim 0.6m$), L_{open} is actually longer near the centre column. This is because B_{ϕ} is higher at smaller R. On the other hand, $< E_{\parallel} >$ increases towards the high field side as the circumference is shortened. As a result, the field lines at $R = 0.23, 0.51$, and 0.8 meet the Townsend break-down condition i.e. $< E_{\parallel} > \geq E_{Townsend}$, whereas the field lines at $1.09m$ and $R = 1.37m$ don't. The comparison at the measured prefill gas pressure at 3ms is also shown over the major radius in Figure 1(b), indicating that the Townsend break-down condition is met only for the high field side i.e. $R = 0.2 \sim 1.05m$. When an open field line meets the Townsend break-down condition, it is assumed that plasma particles are present there, and the volume occupied by the open field line is included in the plasma voume. If field lines are closed, the volume within the closed field lines are also counted. As will be shown later, the plasma volume is dominated by the open field lines at the beginning of break-down, and as plasma current increases, it is gradually taken over by the volume of the closed field lines.

With the modelled plasma volume, the major radius of plasma volume R_{vol} is calculated as the centre of mass, and the minor radius r_{vol} is found by the distance from the major radius to the first

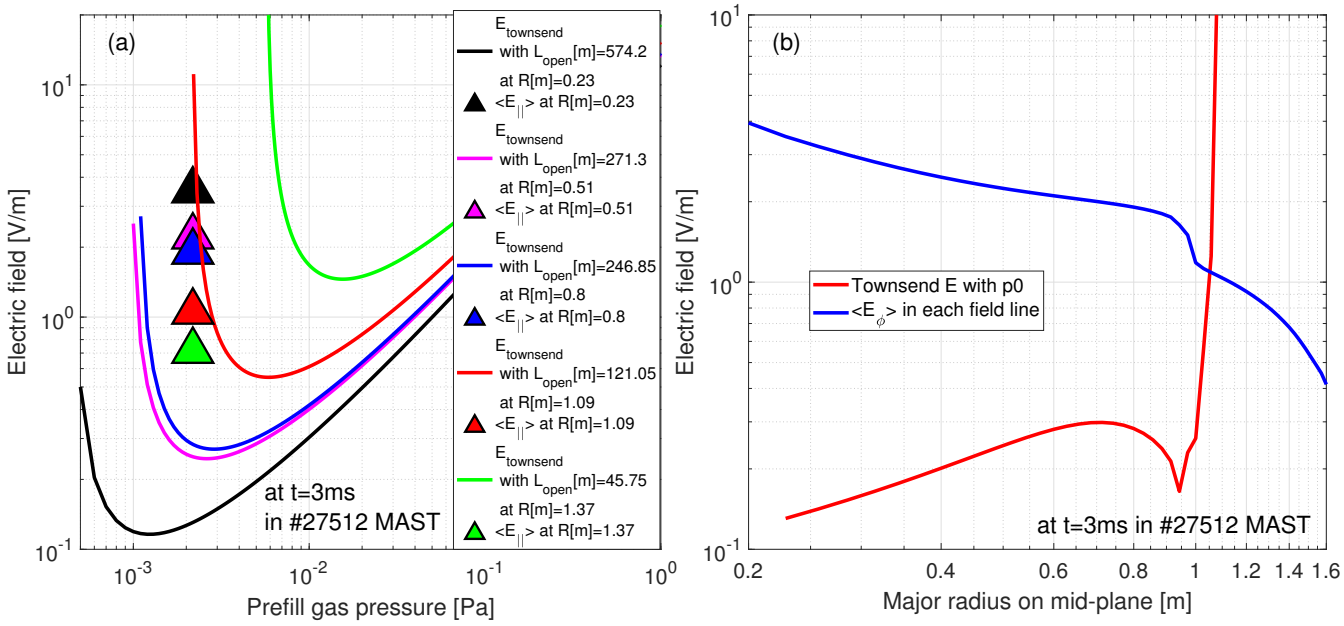

Figure 1: (a)Electric field required for Townsend break-down $E_{townsend}$ (solid lines) and the averaged parallel electric field on each open field line $< E_{\|} >$ (filled triangle) are compared in the range of prefill gas pressure [Torr]. (b) compares $E_{townsend}$ and $< E_{\|} >$ across the major radius position on mid-plane.

wall. The plasma elongation κ is estimated by $\kappa = \big(max(Z_{grid}) - min(Z_{grid})\big)/(2r_{vol})$. The plasma inductance for a conventional tokamak with a large aspect ratio[8] is calculated as:

$$L_p = \mu_0 R_{vol}\big(ln\frac{8R_{vol}}{r_{vol}\kappa^2} + \frac{li}{2} - 2\big) \tag{18}$$

For a spherical torus with a small aspect ratio, the plasma inductance formula is derived in [20] and [21] as:

$$L_p = \mu_0 R_{vol} \times \big(f_A \times \frac{(1-\epsilon)}{1-\epsilon+f_B\kappa} + \frac{l_i}{2}\big) \tag{19}$$

where

$$\begin{aligned} \epsilon &= \frac{r_{vol}}{R_{vol}} \\ f_A &= \big(1 + 1.81\sqrt{\epsilon} + 2.05\epsilon\big)ln(\frac{8}{\epsilon}) - \big(2 + 9.25\sqrt{\epsilon} - 1.21\epsilon\big) \\ f_B &= 0.73(\sqrt{\epsilon}) \times (1 + 2\epsilon^4 - 6\epsilon^5 + 3.7\epsilon^6) \end{aligned} \tag{20}$$

Consistent calculation of L_{open} also improves the confinement time model with a better physics basis than the models used in present burn-through modelling codes (i.e. $L_f = 0.25\times a\frac{B_\phi}{B_z t}exp\Big(\frac{I_p(t)}{I_{ref}}\Big)$[17][22]), in which the evolving connection length during the transition from the open field to closed field lines was estimated by the increase in I_p in the exponential term. In the new confinement time model, the parallel particle transport is calculated with the averaged length of open field lines $< L_{open} >$ and the ratio of the open field lines to the total field lines, and the perpendicular particle transport is calculated with Bohm diffusion:

$$\begin{aligned} \tau_p^{-1} &= \tau_{p,\parallel}^{-1} + \tau_{p,\perp}^{-1} \\ \tau_{p,\parallel} &= \frac{< L_{open} >}{C_s} \times \frac{\#\text{ of open field lines}}{\#\text{ of total field lines}} \text{ where } C_s = \sqrt{\frac{T_e + T_i}{m_D}} \\ \tau_{p,\perp} &= \frac{a}{v_{Bohm}} \text{ where } v_{Bohm} = \frac{1}{8}\frac{T_e[eV]}{a[m]B_\phi[Tesla]} \end{aligned} \tag{21}$$

3 Validation of electromagnetic plasma burn-through model

3.1 Ohmic plasma initiation with direct induction scenario in MAST

There are two plasma initiation scenarios in MAST, namely merging compression and direct induction[23][24]. Figure 2 shows the solenoid and poloidal field coils in MAST. The former scenario was to trigger the plasma break-down near P3 coils by rapidly ramping up the currents in P3 coils and inducing a high loop voltage nearby. The P3 coil current reduces towards $0[A]$ after the peak value, and this makes the two plasma rings merged on the mid-plane. The merged plasma ring is further compressed with P4 and P5 currents to achieve plasma burn-through. After this, the magnetic flux swing in the solenoid induces the loop voltage to increase the plasma current. The latter scenario directly uses the magnetic

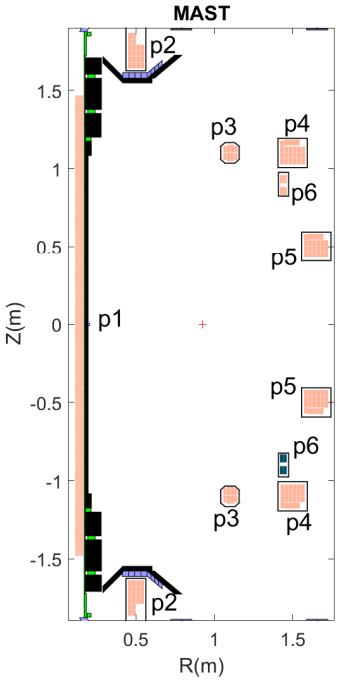

Figure 2: Schematic of solenoid and PF coils (Grey color) in MAST. The toroidally conducting vessel sturctures are in Black color.

flux swing in the solenoid and induces the loop voltage near the magnetic field null. This makes the plasma break-down and burn-through at the null, and also increases the plasma current. Although the merging compression scenario has a benefit of reducing the magnetic flux consumption in the solenoid (i.e. smaller $Volt \times Seconds$) and was well routinely used in most MAST discharges, the merging compression scenario would not be available to use in ITER or STEP as there will be no such in-vessel PF coils. For this reason, we have selected a MAST discharge operated with the direct induction scenario (27512), and performed electromagnetic simulations using the upgraded DYON code.

3.2 Simulation of a MAST discharge

Figure 3 (a) shows the operation currents (i.e. current in a single turn) in the solenoid and PF coils used in #27512. The number of coil turns is indicated in the legend. The effective currents in each coil, which are calculated by the product of the operation currents and the number of coil turns (i.e. amperes $\times$ turns), were given to $\overleftrightarrow{I}_{cvp}$ in (5). The mutual inductance matrix and the resistance matrix corresponding to the MAST design were also given to $\overleftrightarrow{M}_{cvp}$ and $\overleftrightarrow{R}_{cvp}$ in (5), respectively. Solving the full circuit equations, the vessel eddy currents (see Figure 3(b)) and the evolution of 2D poloidal magnetic flux map (see Figure 4) are consistently calculated. The evolving 2D poloidal magnetic flux map is used to calculate the evolving plasma volume with the model described in Section 2.2. As can

be seen in Figure 4, due to the open magnetic field lines, the plasma volume is extended to the vessel wall at the beginning. The plasma volume shrinks to a smaller volume as the plasma current increases and the field lines are closed. The first plasma volume data in EFIT is available from 30ms. At around 30ms, the field lines are also fully closed in DYON modelling results (see Figure 4). The calculated plasma volume agrees well with the EFIT data[25] (see Figure 3(c)). Assuming toroidal symmetry of the plasma geometry, the modelled plasma volume is also used to find the plasma self-inductance and the plasma resistance (Figure 3(d) and (e), respectively). These were used to calculate the plasma current evolution in the full circuit equations. The calculated plasma current agrees well with the measured value, implying the validity of the electromagnetic simulation.

The simulation parameters used in the DYON modelling are summarised in Table 1. As shown in Figure 3(a), the rate of change in the solenoid and PF coil currents before t=-10ms is small, and the the induced vessel eddy currents at around -10ms are small enough to ignore. DYON starts to solve the full circuit equation system from -10ms with the initial condition that the vessel eddy currents in all passive structures are zero. The positive loop voltage at the plasma region starts to increase from 0 seconds. Since the D_α peak appears at 3ms in the photomultiplier tube measurement, the field-line-following calculation and the Townsend break-down model starts to calculate the plasma volume from 3ms, which are used to solve the differential equation system of the plasma energy and particle balance. In the MAST discharge modelling, the field-line-following calculation was performed for the magnetic field lines crossing 50 radial points on the mid-plane at every 1ms.

The initial condition of the electron temperature $T_e(t = 0)$ was assumed as 3eV, and the initial degree of ionization $\gamma(t = 0)$ was consistently calculated as 1% with $\gamma(0) = 2e - 3 \times T_e^{1.5}$[8]. Both the prefilled D_2 molecular gas temperature T_n and the initial Deuterium ion temperature $T_i(t = 0)$ was assumed as the room temperature i.e. 0.026eV. This assumption was used to calculate the density of the prefilled Deuterium atoms with the measured prefill gas pressure [Pa] at 0 seconds:

$$n_D(0)[m^{-3}] = \frac{2 \times p(0)[Pa]}{T_n[eV] \times 1.6e - 19} \tag{22}$$

It was found that use of somewhat lower measured gas pressure improves the agreement with experimental data in #27512. 75% of measured prefill gas was used as input. Since the gas pumping is not modelled, the injected external gas fuelling data, of which the peak value is about $1e22[sec - 1]$, is too high to be used as it is. 10% gas fuelling efficiency was identified for DYON to reproduce the measured parameters in #27512. In addition, the measured gas pressure waveform in #27512 is about 10ms behind the external gas fuelling waveform. Based on this, 10ms delay has been taken into account in the input data of external gas fuelling.

The initial carbon content was assumed to be zero. Since the first wall material in MAST was made of Carbon, Carbon atom influx was calculated with the plasma-wall-interaction model validated against the JET with the carbon wall data in [8], where the chemical sputtering is defined as 0.03. To represent a tiny amount of the impurities remaining from previous dicharges, 0.1% initial oxygen atom content in the prefill gas was assumed as an initial condition. The evolving density of all impurity charge stages was calculated in (12).

The loop voltage induction is a function of the rate of magnetic flux change in a toroidal loop, and thus depends on a loop position (i.e. radius and vertical position). Without an iron core, which is the case in most present devices including MAST, the loop voltage at a plasma position could be different

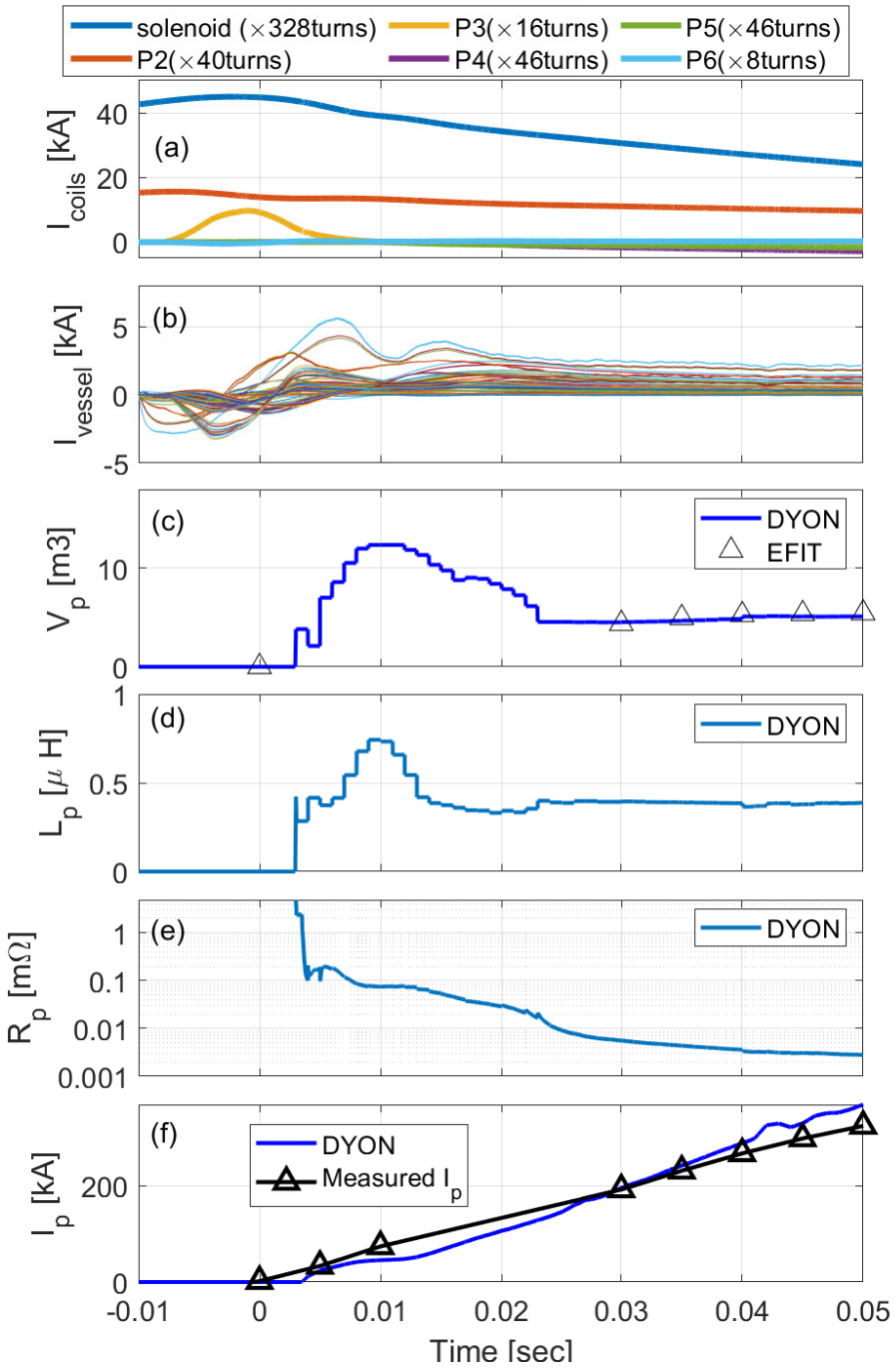

Figure 3: (a)Input coil current trajectories used in DYON (b)Example of vessel eddy currents calculated in each vessel grid in DYON (c)Plasma volume calculated in DYON and in EFIT (d) Plasma self-inductance calculated in DYON (e)Plasma resistance calculated in DYON (f)Plasma current simulated in DYON and measured data

Definition	**Symbol**	**Value**
Simulation time for full circuit equation	t_{EM}	$t = -0.01 \sim 0.5[sec]$
Simulation time for energy and particle balance in a plasma	t_{plasma}	$t = 0.003 \sim 0.5[sec]$
Simulation time for Townsend break-down model	$t_{townsend}$	every $0.001[sec]$ for $t = 0.003 \sim 0.5[sec]$
Number of field lines for field-line-following calculation	$N_{field\,lines}$	50
Initial electron temperature	$T_e(t=0)$	3 [eV]
Initial ion temperature	$T_i(t=0)$	0.026 [eV]
Deuterium atom temperature	T_n	0.026 [eV]
Loop voltage at $R = 0.65[m]$	$V_{loop}(t)$	Modelled (see Figure 5)
Length of open field lines	$L_{open}(t, N)$	Modelled (see (21))
Initial plasma current	$I_p(t=0)$	0 [A]
Vessel eddy currents at -0.01[sec]	$I_v(t=$ -0.01)	0 [A]
Vessel eddy currents at 0[sec]	$I_v(t=0)$	See Figure 3
D_2 gas pressure	$p(t=0)$	1.2 [mPa](= 0.75× measured value)
External D atom fuelling	$\Gamma^{total}_{D,in}(t)$	0.1× Injected rate $[sec^{-1}]$ (in Figure 8)
Initial degree of ionization	$\gamma(t=0)$	0.01
Initial Deuterium atom density	$n^0_D(t=0)$	$5.5e17[m^{-3}]$ (i.e. see (22))
Initial Deuterium ion density	$n^{1+}_D(t=0)$	$5.55e15[m^{-3}]$ (i.e. 1% of $n^0_D(0)$)
Deuterium recycling coefficient	Y^D_D	1
Initial Carbon atom density	$n^0_C(t=0)$	$0[m^{-3}]$
Carbon sputtering yield by D ions	Y^C_D	0.03
Carbon recycling coefficient	Y^C_C	0
Initial Oxygen atom density	n^0_O	$5.55e14[m^{-3}]$ (i.e. 0.1% of $n^0_D(0)$)
Oxygen recycling coefficient	Y^O_O	1
Plasma volume	$V_p(t)$	Modeled (see Figure 4)
Plasma major radius	R_{major}	Modelled (see Figure 4)
Plasma pinor radius	r_{minor}	Modelled (see Figure 4)
Plasma elongation	κ	Modelled (see Figure 4)
Vacuum vessel volume	V_V	$55[m^3]$
Internal inductance of I_p	L_i	0.5 (i.e. uniform J_p profile)
Auxilary heating e.g. ECH	P_{aux}	0[W] (i.e. ohmic burn-through)
Toroidal magnetic field	B_ϕ	0.4[T] at R=1[m]

Table 1: Table of simulation parameters used in DYON modelling for MAST dischargge #27512.

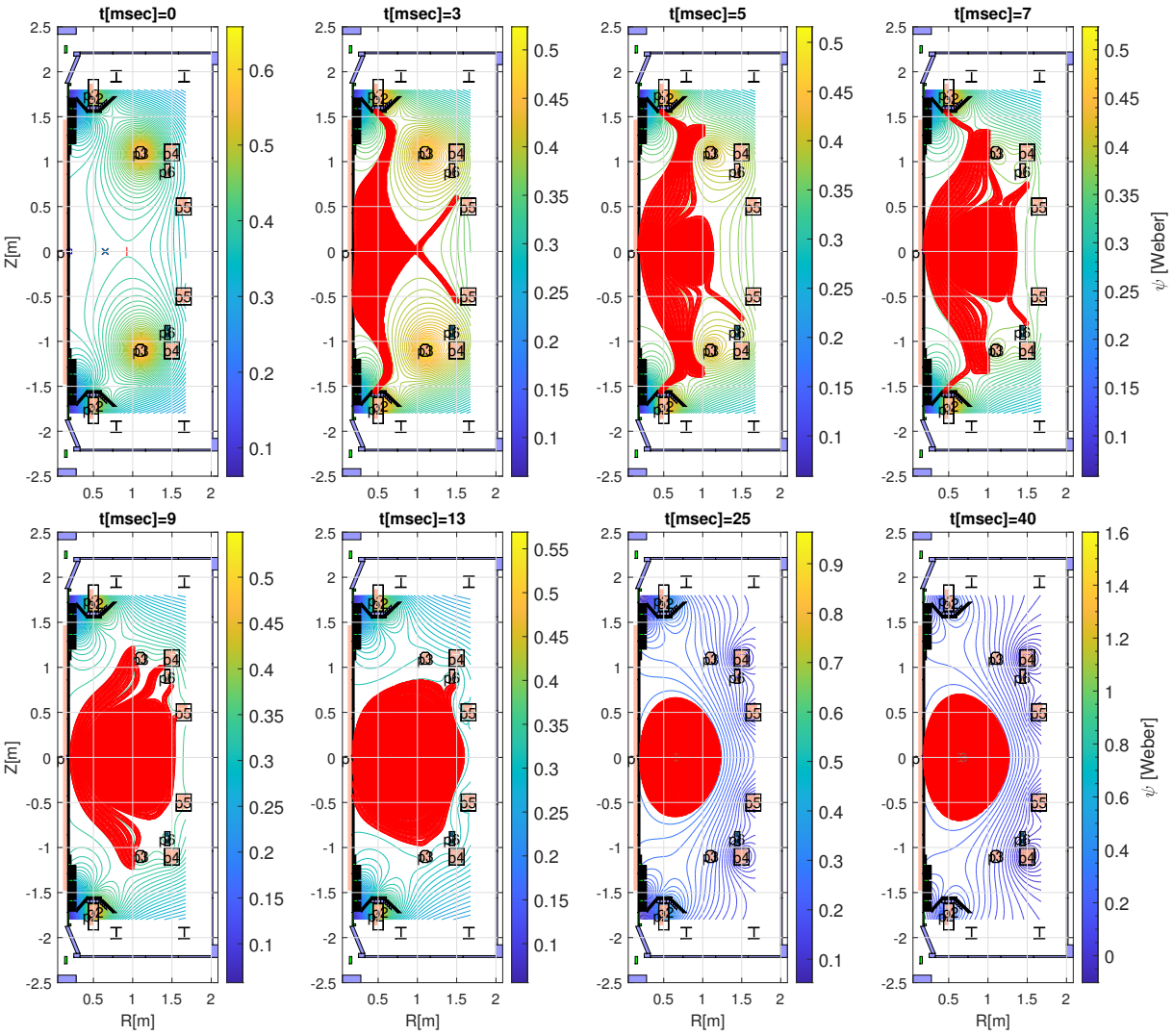

Figure 4: Evolution of plasma volume and ψ map simulated in DYON during the plasma break-down and burn-through phase. The plasma volume model assumes that electrons and ions are located on the magnetic field lines which are closed or meet Townsend criteria.

from the value measured at the vacuum vessel, and it should be calculated by modelling. Figure 5(a) compares the loop voltage at the plasma position calculated by FIESTA[26] and DYON, using the same coil currents in Figure 3(a). The two calculated voltage trajectories almost concide. Considering about a decade of use and validation of FIESTA code in MAST, the good agreement verifies the newly developed electromagnetic model in DYON. The calculated loop voltage at the plasma region can be decomposed to the resistive voltage and the inductive voltage. In Figure 5, the resistive voltage is larger than the inductive voltage until about 22ms. As will be discussed later, 22ms corresponds to the time that carbon is sufficiently ionized so that the line radiation decreases. The validity of the electromagnetic modelling in DYON has also been checked with the flux loop measurement in MAST. Using the 2D psi map evolution in Figure 4, the induced loop voltage was calculated at the positions of magnetic flux loops in MAST. Figure 5(b)(c)(d) show the calculated loop voltages agree well with flux loop measurement at different positions which are the inboard mid-plane (R=0.18m and Z=0.015m, calibration factor = 1.5), upper P3 coil (R=1.1m and Z=1.1m, calibration factor =40), and lower P3 coil (R=1.1m and Z=-1.1m, calibration factor =40), repectively.

So far, validation of plasma burn-through modelling has been only possible with a limited data set, as measured data are usually not available in such an early phase. It is because the main diagnostics system in present devices e.g. Thomson Scattering (TS) is optimized for the flat-top phase where T_e and n_e are high. The Nd:YAG Thomson Scattering (TS) system [27] on MAST operates well for the start-up phase since it is designed to measure a low T_e (from $5eV$) and n_e (from $1e18[m^{-3}]$) using its large collection solid angle. In MAST discharges, measured T_e and n_e are available from very early time e.g. $5[ms]$, and the profile data with high radial resolution covers the break-down and the burn-through phase i.e. $0 \sim 50[ms]$. This provides exceptional data to validate plasma burn-through models. Figure 6(a) and (b) shows the profiles of T_e and n_e measured by MAST TS system, where the line of sight is aligned with the mid-plane. It is worth noting that the first measured profiles of T_e and n_e at $5[ms]$ shows that the plasma initiation takes place from the inboard side, which is qualitatively consistent with the modelled plasma volume in Figure 4. Another useful point to note is that both T_e and n_e profiles are not much centrally peaked. One of the key underlying assumptions in the mainstream plasma burn-through modeling codes (i.e. DYON, BKD0, and SCENPLINT) is that T_e and n_e are uniform across the radius in the burn-through phase. The measured TS profile data justifies this assumption. Figure 6(c) and (d) compares the modelled T_e and n_e in DYON against the time trace of the averaged TS data. The error bars in TS data have been calculated with the root-mean-square of the statistical errors in each radial point. The time evolution of T_e and n_e in DYON is within the experimental error bars, implying the dischage is well simulated in the modelling.

Plasma burn-through modelling could provide useful information to interpret the discharge in the burn-through phase, and to optimize the operation scenario. For example, Figure 7(a) and (b) show how the electrons and ions lose their energy, respectively. At the beginning (i.e $\sim 8[ms]$), electrons lose the energy for the deuterium radiation and the equilibration, which is the heating power to ions. At this time, ions mainly lose the energy for the charge exchange reactions. As can be seen in Figure 7(c), deuterium is fully ionized at around $8[ms]$, and the deuterium radiation and the charge exchange energy loss are reduced. At $15 \sim 20[ms]$, as C^{3+} becomes the dominant charge level, a much larger electron energy loss occurs due to the carbon radiation. The carbon radiation is significantly reduced as the dominant charge level further increases to C^{4+}. After overcoming the carbon radiation, T_e stably increases with the ohmic heating, which allows the plasma current ramp-up.

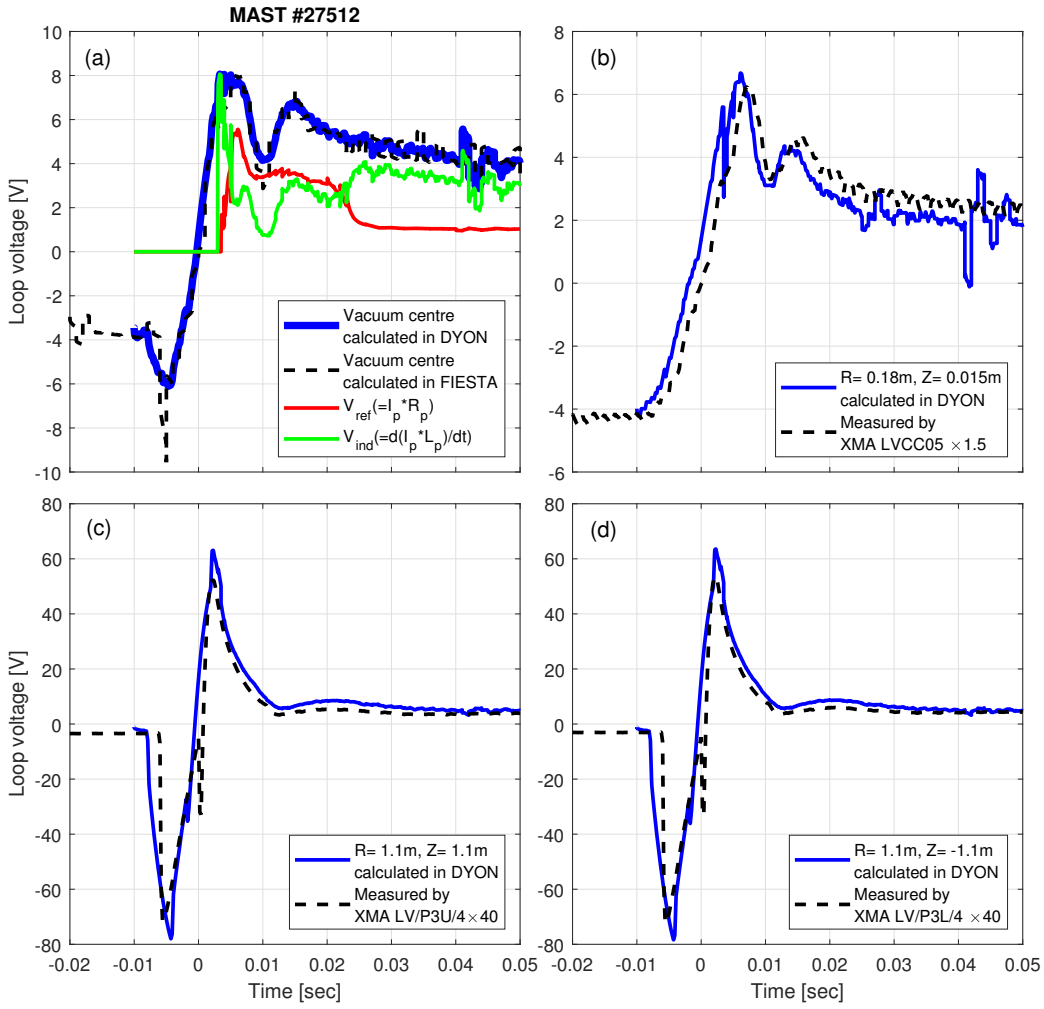

Figure 5: (a)Loop voltage at the plasma position calculated in DYON and FIESTA. (b)(c)(d)Magnetic flux loop data measured in MAST #27512, and corresponding synthetic data calculated in DYON.

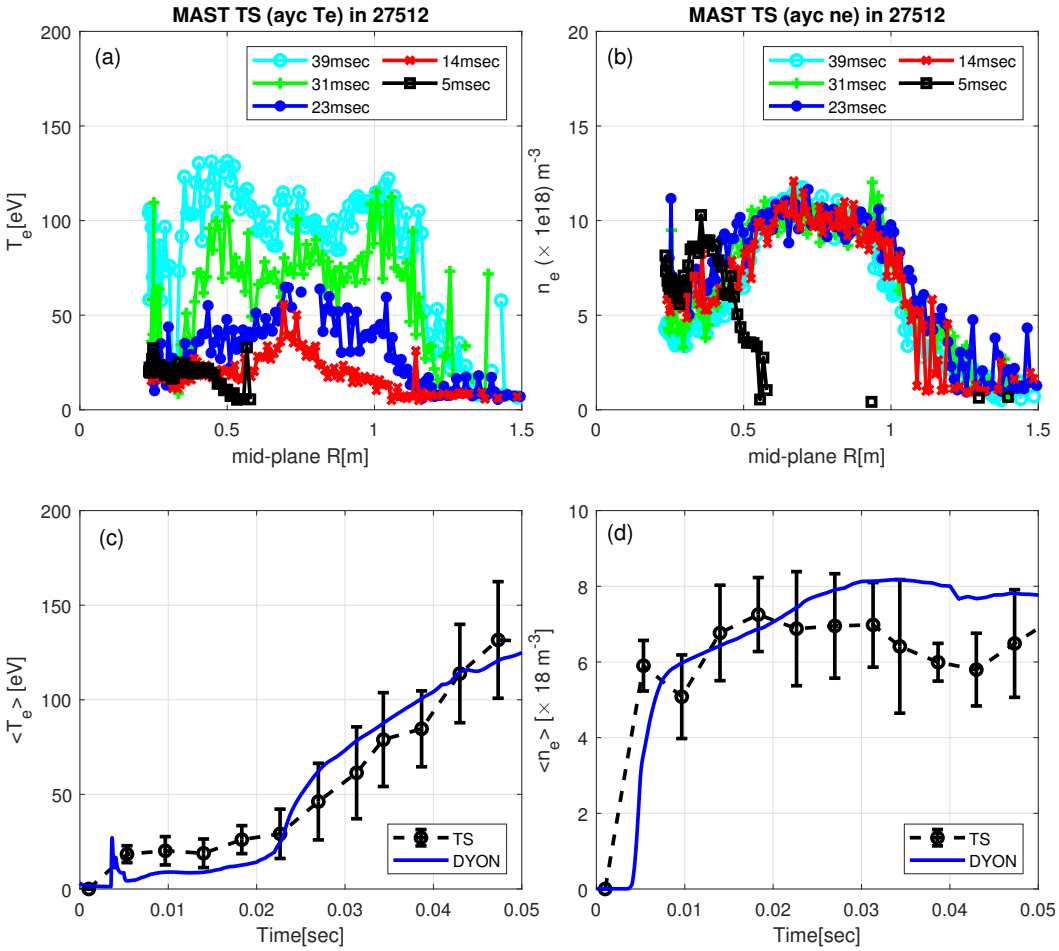

Figure 6: (a)(b)Electron temepreature and density during the plasma burn-through phase, measured by Thomson Scattering in MAST[27] #27512. (c)(d)Comparison of the simulated T_e and n_e in DYON with the line averaged TS T_e and n_e

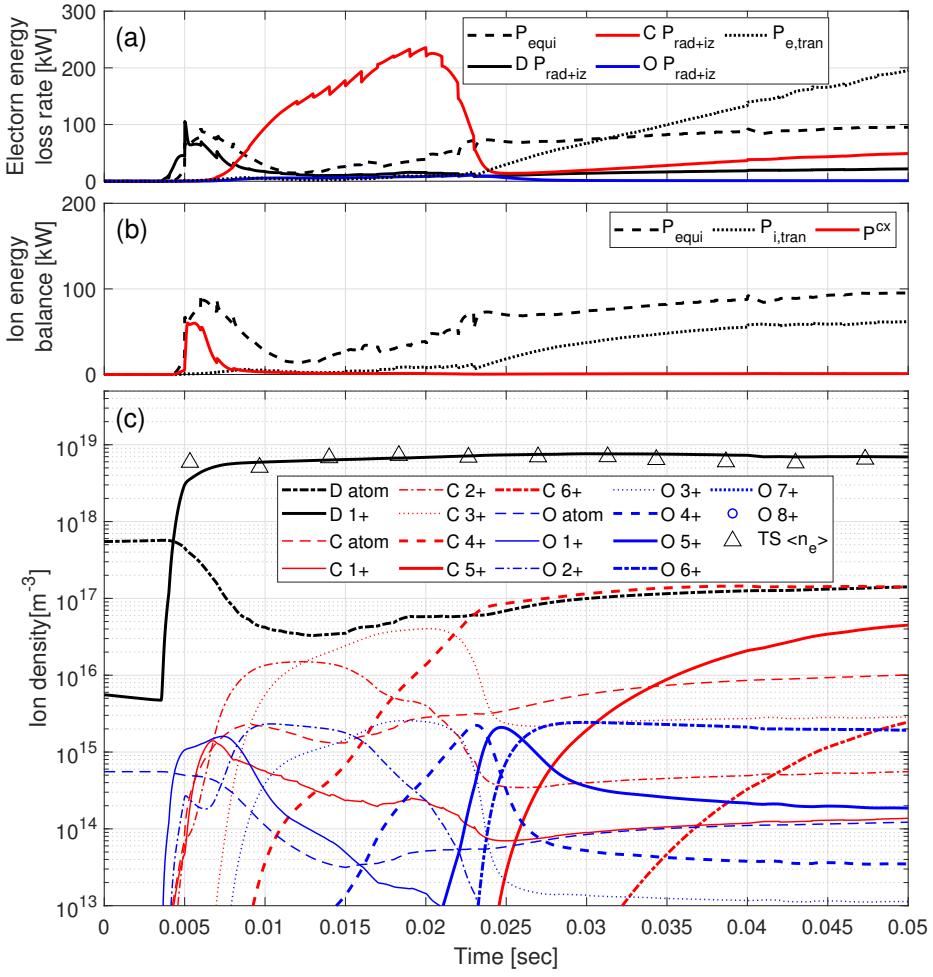

Figure 7: (a)Electron energy loss rate (b)Ion energy loss rate (c)Evolution of ion densities i.e. Deuterium, Carbon, and Oxygen

3.3 Statistical validation

To assess the prediction capability of the electromagnetic DYON modelling, 34 MAST discharges with direct induction ohmic plasma initiation were randomly selected. The same simulation parameters in Table 1 were identically used in all the 34 DYON simulations, and the control room input data such as prefill gas pressure, external gas fuelling rate, and the coil current trajectories in the solenoid and PF coils were individually given from experimental data. Figure 8(a) shows the measured gas pressure in the 34 discharges. The prefill gas pressure at 0 sec is in the range of $1.1 \sim 1.7[mPa]$, and has the peak value at around 15ms due to the external gas fuelling, which was also used as input data. Figure 8(b) shows the loop voltage measured in the flux loop located at the inboard mid-plane (R=0.18m and Z=0.015m). The measured data was multiplied by 1.5 for calibration. The loop voltage waveform is almost identical until 20ms, indicating that the same direct induction scenario was used in all the 34 discharges. Considering that 34 discharges were randomly selected, this reveals that the plasma initiation scenario was only developed when the device was first explored after the construction, and is not further optimized once one recipe working is idenified. This should be the case in most present devices. For better validation of plasma burn-through models, dedicated plasma initiation experiments (e.g. operation parameter scanning for plasma initiation) are required. Among the 34 discharges, 11 discharges start feedback control at around 20ms (the other discharges from 60ms), and the scenarios used after 20ms are varying. Since the modelling was performed until 50ms, the different loop voltage data in 20ms $\sim$ 50ms are still useful for the statistical comparison.

Figure 9 compares I_p, n_e, and T_e calculated by electromagnetic DYON modelling against 34 MAST direct induction ohmic discharges. The colors of triangle symbols represent the time of comparison i.e. blue at 50ms, red at 40ms, cyan at 30ms, and green at 20ms. The plasma currents modelled in DYON agree very well with the measured values at all four comparison times (see Figure 9(a)). The plasma currents at 20ms are all closely gathered at around 120kA in both calculated and measured. This is not surprising as the identical loop voltage data was used until 20ms in all 34 discharges. The different increase in plasma currents are clearer with time. Although the plasma currents of 34 discharges at 50ms are in a much wider range, they are still well reproduced in DYON, providing the confidence in I_p ramp rate prediction in the burn-through phase.

The electron temperature calculated also reasonably agrees with TS measured electron temperature (see Figure 9(c)), implying the plasma resistivity calculation should be in reasonable agreement as well. Compared to the very good agreement in the plasma currents, the scatter in Figure 9(c) is larger. This could be due to the TS error bars as shown in Figure 6(c) (e.g. 30eV at 50ms). Most electron densities in 34 discharges at the four comparison time are in the range of $5 \sim 10e18m^{-3}$. As can also be seen by TS measurement in Figure 6(d), electron densities in 34 discharges rapidly increase until 20ms, but do not further increase after 20ms. A few discharges have measured densities higher than $12e18[m^{-3}]$. They correspond to the discharges with high external gas fuelling, which is also indicated by the increase in the gas pressure after 30ms in Figure 8(a). Since the external gas fuelling is one of the input data in the modelling, the increase in electron density is qualitatively reproduced in the calculated density, although they are about 30% undercalculated (see Figure 9(b)). This could be partly due to the TS error bars (see Figure 6(d)) and also the uncertainty in the effective gas fuelling coefficient, which is assumed as 10% in the present modelling.

Finally, Figure 9(d) compares the calculated volume in DYON against the EFIT plasma volume. The first data of plasma volume in EFIT is available at 40ms, which is the time that the closed flux

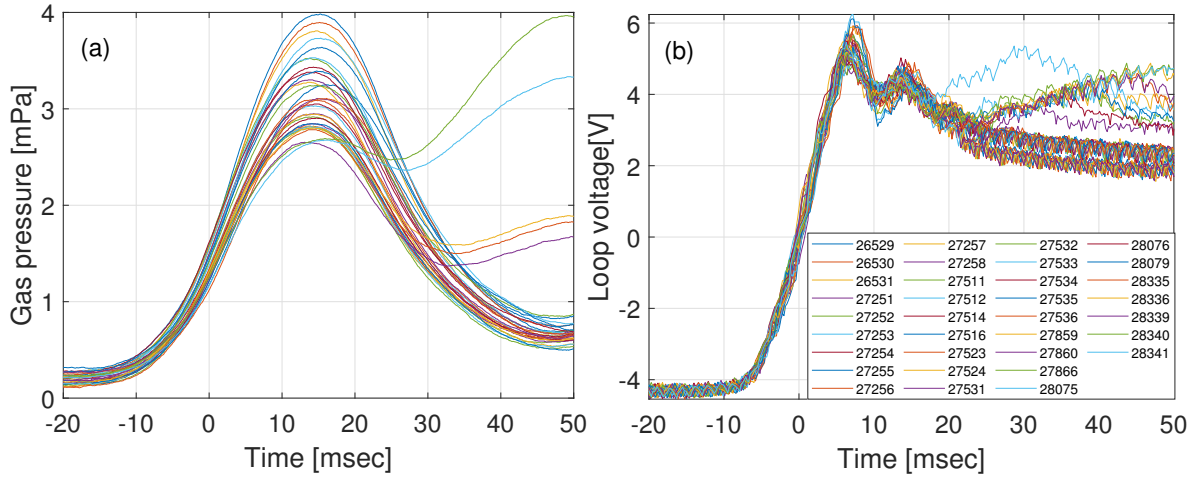

Figure 8: Control room operation parameters used in the 34 MAST discharges with direct induction start-up : (a) Measured gas pressure (b) Measured loop votage in the flux loop at the inboard mid-plane (R=0.18m, Z=0.015m, calibrated by $\times 1.5$)

surfaces are fully formed. As shown in Figure 4, field lines at 40ms are also fully closed in DYON modelling and the calculated volume agree very well with the EFIT data. For complete validation of the plasma volume model, measurement of plasma volume with open field lines is required. This would require a dedicated experiments or novel processing of fast camera images.

4 Conclusion

Following the lesson learnt from the ITPA-IOS joint activity of plasma burn-through simulation code benchmark [17], we have developed full circuit equations and plasma volume model in DYON. The mathmatical derivation of the electromagnetic plasma burn-through model has been provided in this paper. The electromagnetic model enables plasma burn-through simulations only with the control room operation parameters such as coil currents (or voltages) in solenoid and PF coils and prefill gas pressure. This new feature is necessary to perform predictive simulations and optimize operation scenarios in a future device such as ITER and STEP. In addition, the plasma volume evolution during the burn-through phase can now be consistenly calculated with the physics-based model, reducing one of the main uncertainties that plasma burn-through modelling has had so far. The upgraded plasma burn-through model has successfully reproduced 34 MAST discharge with the direct induction scenario, indicating the validity of the developed model and the prediction capability. For more complete validation, dedicated experiments with operation parameter scanning and measurement of plasma volume with open field configuration are needed. It will improve the confidence when using the electromagnetic plasma burn-through model to optimize ITER operation scenarios and to design STEP.

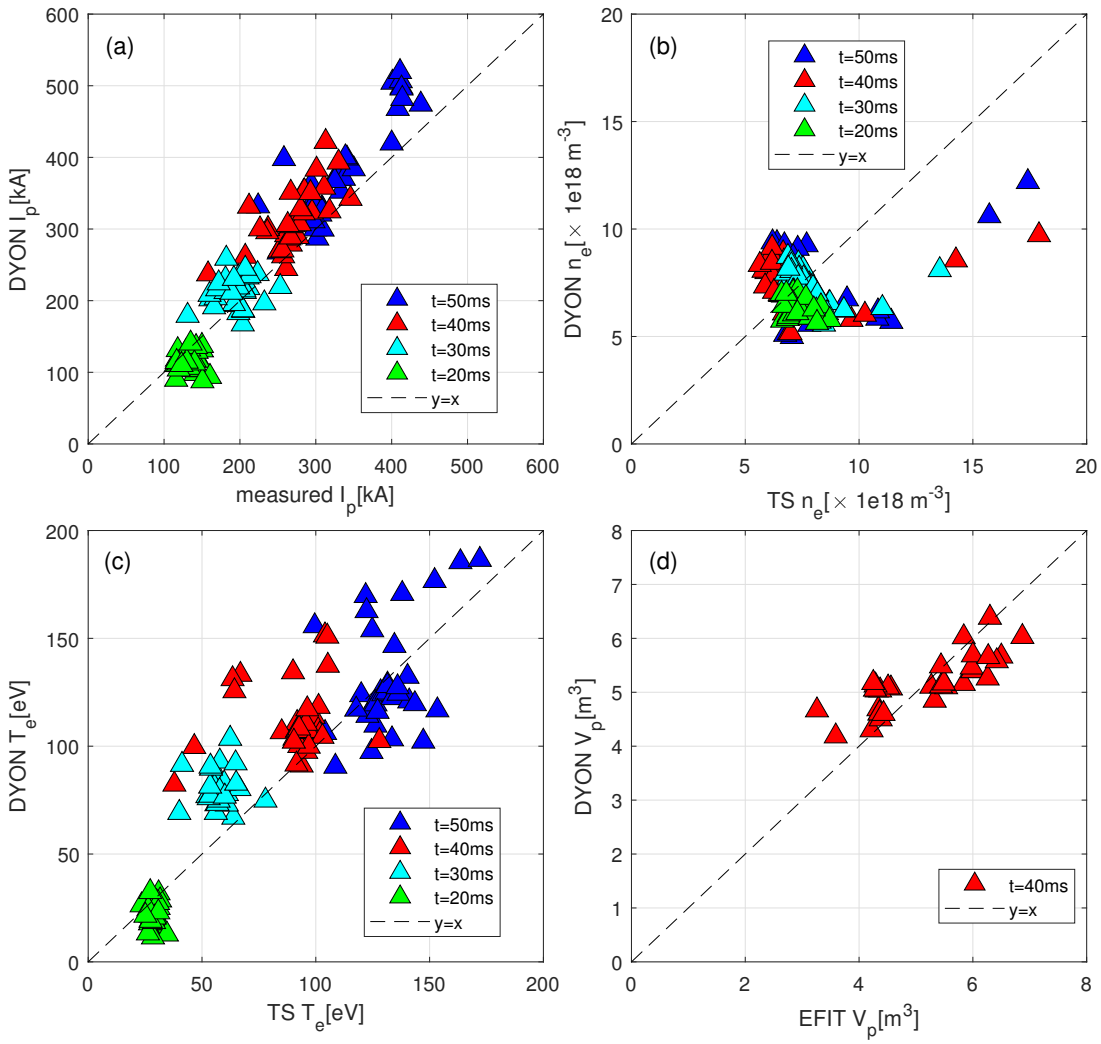

Figure 9: Statistical comparison of the parameter evolution in time between DYON and measurement: (a) plasma current (b) electron density (c) electron temperature, and (d) plasma volume. Each symbol indicates the time for comparison. TS stands for Thomson Scattering measurement. The first data of plasma volume in EFIT is available for $30 \sim 40$ms.

Acknowledgement

This work has been carried out within the framework of the EUROfusion Consortium, funded by the European Union via the Euratom Research and Training Programme (Grant Agreement No 101052200 — EUROfusion) and from the EPSRC [grant number EP/W006839/1]. To obtain further information on the data and models underlying this paper please contact PublicationsManager@ukaea.uk. Views and opinions expressed are however those of the author(s) only and do not necessarily reflect those of the European Union or the European Commission. Neither the European Union nor the European Commission can be held responsible for them.

References

[1] R Papoular 1976 *Nucl. Fusion* **16** 37–45 URL https://doi.org/10.1088/0029-5515/16/1/004

[2] B Lloyd 1991 *Nucl. Fusion* **31** 2031–53 URL https://doi.org/10.1088/0029-5515/31/11/001

[3] H Summers OPEN-ADAS URL https://open.adas.ac.uk/

[4] R J Hawryluk 1976 *Nucl. Fusion* **16** 775 URL https://doi.org/10.1088/0029-5515/16/5/005

[5] ITER Physics Expert Group 1999 *Nucl. Fusion* **39** 2577 URL https://doi.org/10.1088/0029-5515/39/12/308

[6] P C de Vries 2019 *Nucl. Fusion* **59** 096043 URL https://doi.org/10.1088/1741-4326/ab2ef4

[7] URL https://step.ukaea.uk/

[8] Hyun-Tae Kim 2012 *Nucl. Fusion* **52** 103016 URL https://doi.org/10.1088/0029-5515/52/10/103016

[9] Hyun-Tae Kim 2013 *Nucl. Fusion* **53** 083024 URL https://doi.org/10.1088/0029-5515/53/8/083024

[10] Hyun-Tae Kim 2013 *Plasma Phys. Control. Fusion* **55** 124032 URL https://doi.org/10.1088/0741-3335/55/12/124032

[11] Y Gribov 2007 *Nucl. Fusion* **47** S385 URL https://doi.org/10.1088/0029-5515/47/6/S08

[12] V A Belyakov 2003 Analysis of initial stage of plasma discharge in tokamaks: mathematical model formulation, simulation results, comparison with experiments *Int. Conf. on Physics and Control* vol 3 pp 1025–34 URL https://doi.org/10.1109/PHYCON.2003.1237045

[13] A B Mineev 2014 Study of iter first plasma initiation using a 3d electromagnetic model URL https://conferences.iaea.org/event/46/contributions/8477/

[14] G Granucci 2015 *Nucl. Fusion* **55** URL https://doi.org/10.1088/0029-5515/55/9/093025

[15] D Ricci 2016 Operational parameters for ec assisted start-up in iter URL http://ocs.ciemat.es/EPS2016PAP/pdf/O5.130.pdf

[16] D Ricci 2018 Discharge recovery by means of ec assisted start-up URL http://ocs.ciemat.es/EPS2018PAP/pdf/P4.1074.pdf

[17] Hyun-Tae Kim 2020 *Nuclear Fusion* **60** 126049 URL https://doi.org/10.1088/1741-4326/abb95c

[18] Hyun-Tae Kim 2013 Physics and computational simulations of plasma burn-through for tokamak start-up Imperial College London PhD Thesis URL https://spiral.imperial.ac.uk/handle/10044/1/18082

[19] Hyun-Tae Kim 2013 *J. Nucl. Mater.* **438** S1271 URL https://doi.org/10.1016/j.jnucmat.2013.01.056

[20] S P Hirshman 1986 *Physics of Fluids* **29** 790 URL http://dx.doi.org/10.1063/1.865934

[21] Seong-Cheol Kim 2022 *Nuclear Fusion* To be submitted

[22] B Lloyd 1996 *Plasma Phys. Control. Fusion* **38** 1627 URL https://doi.org/10.1088/0741-3335/38/9/007

[23] A Sykes 2001 *Nuclear Fusion* **41** 1423 URL https://doi.org/10.1088/0029-5515/41/10/310

[24] D J Battaglia 2019 *Nuclear Fusion* **59** 126016 URL https://doi.org/10.1088/1741-4326/ab3bd5

[25] L L Lao 1985 *Nuclear Fusion* URL https://iopscience.iop.org/article/10.1088/0029-5515/25/11/007/meta

[26] G Cunningham 2013 *Fusion Engineering and Design* **88** 3238–3247 URL http://dx.doi.org/10.1016/j.fusengdes.2013.10.001

[27] R Scannell 2010 *Review of Scientific Instruments* **81** 10D520 URL https://doi.org/10.1063/1.3460628